

Ultra-fast magnetic resonance encephalography of physiological brain activity – Glymphatic pulsation mechanisms?

Vesa Kiviniemi^{1,2}, Xindi Wang^{1,2,3}, Vesa Korhonen^{1,2},
Tuija Keinänen^{1,2}, Timo Tuovinen^{1,2}, Joonas Autio^{1,4},
Pierre LeVan⁵, Shella Keilholz⁶, Yu-Feng Zang⁷, Jürgen Hennig⁵
and Maiken Nedergaard⁸

Journal of Cerebral Blood Flow & Metabolism
2016, Vol. 36(6) 1033–1045
© Author(s) 2015
Reprints and permissions:
sagepub.co.uk/journalsPermissions.nav
DOI: 10.1177/0271678X15622047
jcbfm.sagepub.com



Abstract

The theory on the glymphatic convection mechanism of cerebrospinal fluid holds that cardiac pulsations in part pump cerebrospinal fluid from the peri-arterial spaces through the extracellular tissue into the peri-venous spaces facilitated by aquaporin water channels. Since cardiac pulses cannot be the sole mechanism of glymphatic propulsion, we searched for additional cerebrospinal fluid pulsations in the human brain with ultra-fast magnetic resonance encephalography. We detected three types of physiological mechanisms affecting cerebral cerebrospinal fluid pulsations: cardiac, respiratory, and very low frequency pulsations. The cardiac pulsations induce a negative magnetic resonance encephalography signal change in peri-arterial regions that extends centrifugally and covers the brain in ≈ 1 Hz cycles. The respiratory ≈ 0.3 Hz pulsations are centripetal periodical pulses that occur dominantly in peri-venous areas. The third type of pulsation was very low frequency (VLF 0.001–0.023 Hz) and low frequency (LF 0.023–0.73 Hz) waves that both propagate with unique spatiotemporal patterns. Our findings using critically sampled magnetic resonance encephalography open a new view into cerebral fluid dynamics. Since glymphatic system failure may precede protein accumulations in diseases such as Alzheimer's dementia, this methodological advance offers a novel approach to image brain fluid dynamics that potentially can enable early detection and intervention in neurodegenerative diseases.

Keywords

Resting state, glymphatics, magnetic resonance encephalography, cardiorespiratory, blood oxygen level dependent

Received 30 June 2015; Revised 4 November 2015; Accepted 6 November 2015

Introduction

Recently, the lymphatic draining system of the brain tissue, also called glymphatic system, was described as convection of cerebrospinal fluid (CSF) between the peri-arterial and peri-venous spaces.^{1,2} The driving

⁵Medical Physics, Department of Radiology, University Medical Center Freiburg, Freiburg, Germany

⁶Wallace H. Coulter Department of Biomedical Engineering, Georgia Institute of Technology and Emory University School of Medicine, Atlanta, GA, USA

⁷Center for Cognition and Brain Disorders, Hangzhou Normal University, Hangzhou, China

⁸School of Medicine and Dentistry, University of Rochester Medical Center, Rochester, NY, USA

¹Oulu Functional NeuroImaging, Department of Diagnostic Radiology, MRC, Oulu University Hospital, Oulu, Finland

²Medical Imaging, Physics and Technology, the Faculty of Medicine, University of Oulu, Oulu, Finland

³State Key Laboratory of Cognitive Neuroscience and Learning & IDG/McGovern Institute for Brain Research, Beijing Normal University, Beijing, China

⁴Functional Architecture Team, Center for Life Science Technologies, RIKEN, Japan

Corresponding author:

Vesa Kiviniemi, Department of Diagnostic Radiology, Oulu University Hospital, P.O. Box 50, Oulu 90029, Finland.
Email: vesa.kiviniemi@oulu.fi

motor of the convective flow was in part related to the cardiac-induced blood flow pulsations along the arteries.^{3,4} Arterial pulsations propulse water through aquaporin channels and support solute transport from the periarterial Virchow–Rubin spaces into the extracellular brain tissue.^{1,2} Then, convective flow pulses migrate through the brain tissue and flush fluid into peri-venous space. The peri-venous spaces conduit waste products from the brain into the lymphatic system. Outside the brain parenchyma, a recent study has demonstrated the existence of regular lymph vessels in meningeal membranes that then conveys debris along effluxed CSF from the glymphatic system.⁵

Iliff et al. have shown that the propulsive energy of arterial pulsation in part drives the glymphatic CSF convective system.⁴ However, the cardiac pulsation provides no more than 15–25% of the propulsive energy and other pulsation mechanisms must contribute to the convective CSF fluid dynamics.⁶ Early functional magnetic resonance imaging (fMRI) scans and other modalities have shown that there may be several sources of pulsations in the brain.^{7–11} The spectrum of susceptibility-weighted blood oxygen level dependent (BOLD) signals shows a $1/f$ frequency profile with most pulsatile power in very low frequencies (< 0.1 Hz) and distinct respiratory rate (0.2–0.3 Hz) and cardiac frequency (0.8–1.2 Hz) peaks.⁹ The brain also experiences a jerk from the arteries during cardiovascular pulsations, which induces movement in the brain.¹¹

Previously, the different pulsations have been mostly regarded as noise obscuring the targeted neurovascular activation responses in the BOLD signal and great efforts have been taken in order to minimize their effects.^{12–15} BOLD signal fluctuations < 0.1 Hz have been linked to functional connectivity of brain networks and vasomotor waves.^{7,8,16–19} Much of the interactions and mechanisms of these pulsations affecting the cerebral BOLD signal still remain unclear. One reason for the uncertainty of BOLD signal pulsations is the fact that whole-brain fMRI studies sample data slowly, i.e. one brain volume in 2–3 s. This results in aliased pulsations from faster frequencies to slower ones. Motion occurring between subsequent magnetic resonance (MR) image slices induces spin-history changes that are difficult to correct.²⁰ The combined effects of aliasing with motion-related spin-history issues prevent the direct visualization of the spatiotemporal characteristics of pulsations with whole-brain BOLD scans.

Recent ultra-fast 3D k-space undersampling techniques like magnetic resonance encephalography (MREG) can image the whole brain in 100 ms. This enables a critical removal of cardiorespiratory aliasing and inherently the 3D measurement helps to avoid spin-history artifacts that otherwise occur in sequential 2D acquisitions due to bulk head motion across 2D slices.^{21,22} MREG with

synchronous electro- and cardiorespiratory monitoring can thus image the temporal evolution of all physiological pulsations with 3D whole-brain coverage.²³ Animal experiments even with dedicated scanners currently cannot perform this due to the fast frequency of cardiorespiratory pulsations compared to the image sampling rate. Novel image analysis algorithms can further effectively separate periodic pulsations of the brain in order to characterize their spatiotemporal patterns over a wide range of frequencies.^{17,19}

In this study, a collaborative effort was undertaken to comprehensively monitor the spatiotemporal effects of physiological pulsations in brain tissue with novel multimodal ultra-fast MREG technology. This technology removes aliasing and minimizes motion-induced spin-history effects and offers increased statistical power for analysis. We hypothesized that low-frequency vasomotor waves are not merely aliased cardiorespiratory pulsations but rather form their own spatiotemporal pattern. We show for the first time distinct patterns of cardiac, respiratory, and vasomotor pulsation patterns and follow how these propagate in the human brain. New results and ideas with regards to physiological pulse quantitation are presented and discussed with respect to glymphatic mechanisms as a primary model for CSF flow dynamics during resting state.

Methods

The ethical committee of the Ostrobothnia district approved the study. Written informed consent of the healthy subjects was obtained according to the declaration of Helsinki. Nine healthy subjects were imaged (5 females, 25.67 ± 4.52 years).

Magnetic resonance imaging scanner

Subjects were scanned using a Siemens 3T SKYRA with a 32-channel head coil. We utilize an MREG sequence obtained from Freiburg University. Briefly, the sequence excites a 192 mm thick slab, thus covering the entire brain, and uses a single-shot stack-of-spirals trajectory to cover 3D k-space in an undersampled fashion in less than 100 ms and at a resolution of $3 \times 3 \times 3$ mm³ (3D matrix size $64 \times 64 \times 64$).²² Undersampling is then resolved by expressing the data acquired by each single coil element as a non-uniform Fourier transform of the original image and inverting the resulting parallel imaging problem using a conjugate gradient algorithm. This resulted in the following scanning parameters: TR 100 ms, TE 36 ms, flip angle 25°, and offers thus about 20–25 times faster scanning than conventional fMRI. The subjects were scanned for 10 min, i.e. 5822 3D brain volumes were obtained after removal of initial T1-saturation effects. Also note that due to the high

sampling rate, this amount of MREG data from nine subjects yields as many data points as in 173 subjects recorded with a classical $TR=2s$ for the same 10 min period in 3 mm voxels. 3D MPRAGE (TR 1900 ms, TE 2.49 ms, TI 900 ms, flip angle 9° , FOV 240, 0.9 mm) cubic voxel images were used to register the MREG data onto 4 mm Montreal Neurologic Institute space (MNI). The magnetic resonance imaging (MRI) scanner t-pulses and optic pulse were used as to synchronize all scanned signals. Respiratory data were acquired using the scanner's pneumatic respiratory monitoring belt to discriminate the frequency bands related to respiration. Other physiological data were obtained using a MRI-compatible synchronous multimodal neuroimaging system fitted to the 3T Skyra imaging room.²³

Cardiovascular and respiratory signal processing

The cardiac cycle information was detected from the brain products MRI-compatible electrocardiographic

(ECG) lead signal to identify the heart beat rhythm.²³ MREG imaging-induced gradient and ballistocardiographic artefacts were removed using Brain Analyser software. This was followed by removal of linear and quadratic trends. Cardiac R-peaks from the filtered ECG data were used as subsequent triggers since they proved most robustly detectable after band-pass filtering from the ECG signal obtained during scanning. The subject-specific ECG data were used to get cardiac frequency bands ($Card_{freq} \approx 0.8\text{--}1.2\text{ Hz}$) for subsequent band-pass filtering of each subject's MREG data, see also Figure 2. The filtered ECG signal was then analyzed with the Matlab findpeaks-algorithm to obtain the timing of individual cardiac R-peaks for initiating pulsation analysis of the band-pass filtered MREG data.

Subject-specific respiratory signal data recorded by the scanner's pneumatic respiratory monitoring belt were also corrected for linear and quadratic trends. Individual window length (WL) was also calculated for each subject according to his or her respiratory

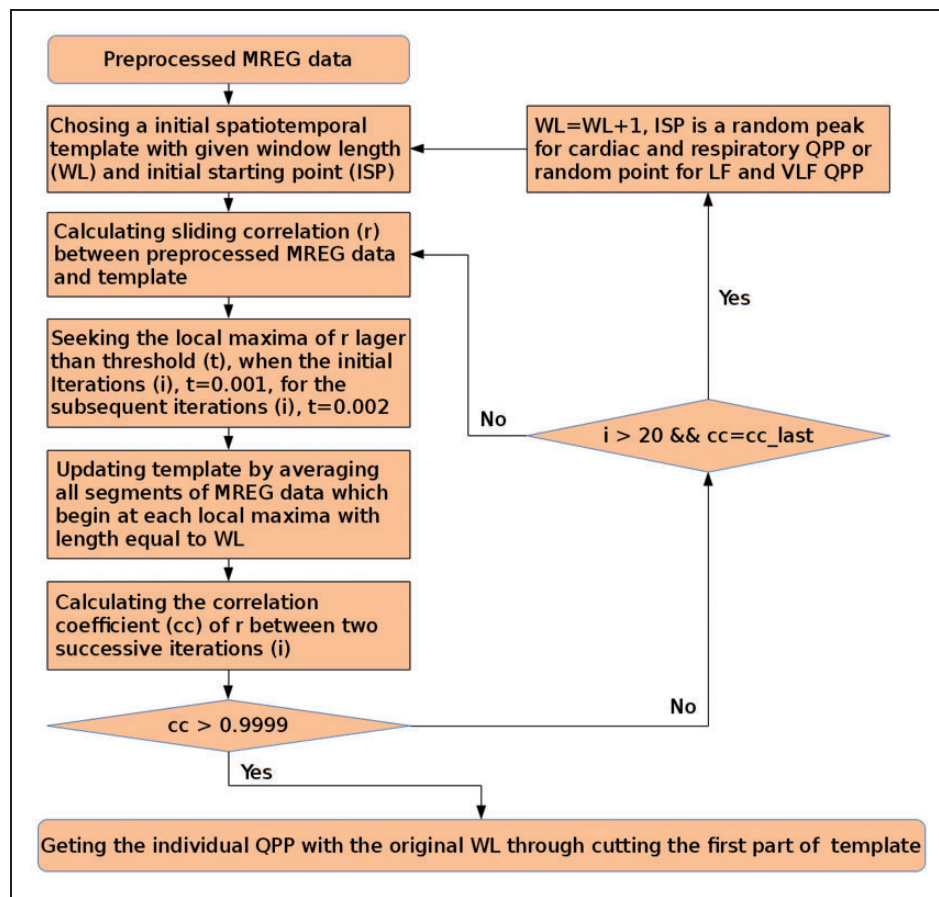


Figure 1. Illustration of the iterative QPP algorithm procedure in the detection of both periodic and quasi-periodic physiological brain pulsations.

rate ($\text{Resp}_{\text{freq}} \approx 0.15\text{--}0.35\text{ Hz}$), c.f. Figure 2. Finally, the averaged respiration periods were used as WL, and initial respiratory peak points identified from MNI coordinates (0, -36.14) in MREG data were considered as the initial starting point (ISP) for periodic pulse averaging in the quasi-periodic pulsation (QPP) algorithm. Individual averaged MREG images at each phase of the cardiac and respiratory cycles were normalized to subject #9's respective data and presented as averaged maps of cardiac (Card_{map}) and respiratory (Resp_{map}) pulsations. As a validation, the ICA components of arterial and CSF pulsations, MRI-compatible Aestiva/5 MRI, Datex Ohmeda anesthesia monitor data, and MCFLIRT head motion parameters were used to verify correct cardiac and respiratory rhythms in MREG data from the multimodal data.

Low-frequency signal processing

The very low frequency (VLF; 0.01–0.027 Hz) and low-frequency (LF; 0.027–0.073 Hz) time vectors were identified from the MREG data resting state ventromedial prefrontal part of the default mode network (DMN_{vmpf}) IC component. The DMN_{vmpf} was detected from the MREG data with FSL 5.0 Melodic using group PICA as previously described.²³ We separated 100 IC's and used dual regression to derive the DMN_{vmpf} signal from the MREG data for minimizing autocorrelation effects. VLF and LF ranges were chosen since they have differential effects on the blood flow physiology of the brain.^{24–26} Based on the minimum frequencies of 0.027 Hz and 0.01 Hz, WL of 37 s for LF and 100 s for VLF were chosen, respectively. Low-frequency blood pressure wave analysis was based on non-invasive blood pressure (NIBP) data collected in synchrony with MREG.²³

MREG data pre-processing

The MREG data were anatomically registered onto individual T1-weighted structural images with the functional data registration tool FLIRT available from the Oxford University fMRIB Software Library (FSL: www.fmrib.ox.ac.uk/fsl). Most of the MREG data pre-processing steps for periodical pulsation data were performed using AFNI-software.^{27,28} After removing the first 100 volumes, the first 3000 volumes (5 min) of MREG data were utilized in this study in order to reduce the amount of calculation. Motion correction was performed with FSL MCFLIRT-software, followed by spatial smoothing with a 6 mm Gaussian kernel (3dBlurInMask). The 3–4% signal slow drift due to scanning-induced warming effects present in all scanners was removed by regression of linear and quadratic temporal trends performed on all the datasets.²⁹

Then, based on subject-specific $\text{Card}_{\text{freq}}$, $\text{Resp}_{\text{freq}}$, and general LF and VLF bands, temporal band-pass filters (3dbandpass) were applied in order to get four individual MREG datasets for each subject that contained only the targeted physiological pulsation frequencies. The filtered data were analyzed for periodic pulsations separately with the averaging algorithm described below. The percent signal change ($(S_{\text{min}} - S_{\text{max}}) / S_{\text{mean}}$) of each pulse was calculated from each ROI individually and averaged on a group level.

Detection of periodic and QPP maps – The QPP_{maps}

Periodic cardiac (Card_{map}) and respiratory (Resp_{map}), as well as QPP spatial pattern maps in the LF (LF_{map}) and VLF (VLF_{map}) bands of the brain were detected using a similar QPP algorithm as Shella Keilholz's group previously.^{17–19} The QPP algorithm uses a data-driven and correlation-based approach to find high SNR (quasi-) periodic, repeating spatiotemporal patterns (like cardiac impulse, respiratory rhythms and LF/VLF fluctuations) from the band-passed MREG brain data, c.f. Figure 2.

The algorithm iteratively seeks QPP_{maps}, which have the maximum *spatial* correlation with a prior of the periodic event in the data. In our study, the QPP algorithm was given a predefined WL that was identified from the measured physiological data as described above. The QPP algorithm parameters are as follows: correlation coefficient (cc) > 0.9999, the threshold of correlation for the initial three steps is 0.001, followed by 0.002 for the subsequent steps. However, there were some modification within iteration: if cc cannot get a value larger than 0.9999 ($\text{cc}_{\text{last}} = \text{cc}$, or 20 times' iteration), WL will perform a self-add operation, and then restart a iteration with new WL until $\text{cc} > 0.9999$, then we cut these QPP's results with original WL as the targeted QPP. The QPP algorithm is presented in Figure 2.

Physiological triggers

In contrast to previous studies,¹⁷ our initial cardiac cycle QPP prior started from a synchronized R-peak based on the ECG physiological measurements, which was synchronized with the MREG scan. This way we were able to synchronize our averaged cardiac MREG maps (Card_{map}) to each individual's systolic phase in the cardiac cycle. From thereon, the QPP algorithm finds successive heart impulses and averages them together as a map. For Resp_{map} period detection, we selected a voxel with clear respiratory pulsation in MREG signal peak in the corpus callosum (2 mm MNI coordinates 0, -36.14) near ventricles. The MREG signal peak from corpus callosum was verified

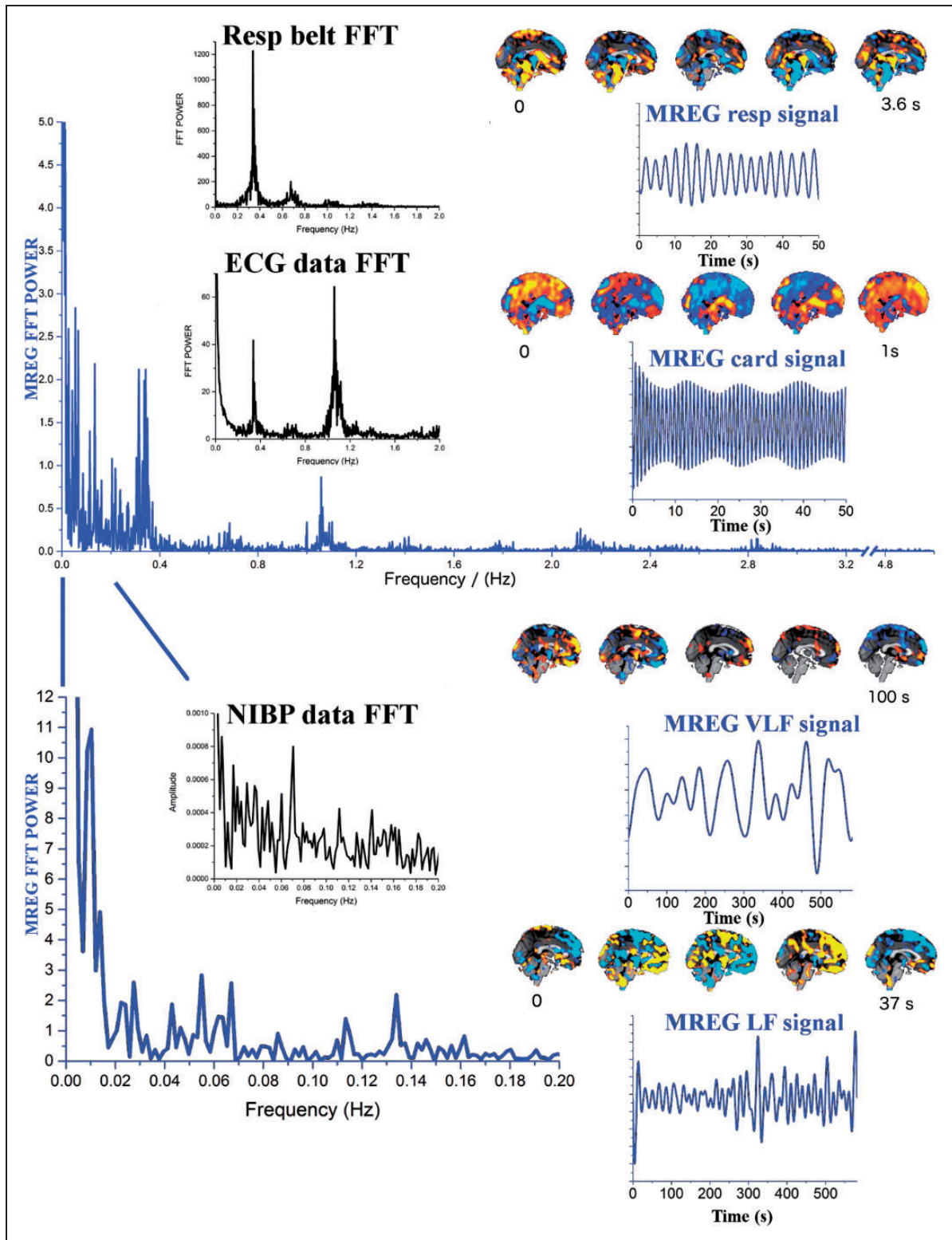


Figure 2. Illustrates two blue MREG Fast Fourier Transform (FFT) power spectra of a ventromedial DMN_{vmpf} MREG time signal after PICA-dual regression. The upper presents power till 5 Hz (cut-off 3.2–4.8 Hz) and below between 0–0.2 Hz. Respiratory frequency clusters around 0.37 Hz and cardiac frequency peaks at 1.08 Hz in MREG data, which are identical to pneumatic respiratory monitoring belt and FFT power spectra of ECG data shown in black. The cardiorespiratory pulsations have harmonic peaks at higher frequencies both in MREG and physiological verification data. VLF (0.01–0.027 Hz) and LF (0.027–0.73 Hz) bands present highest power peaks in the spectrum. NIBP data are shown to illustrate VLF/LF spectral power of the mean arterial blood pressure waves. The filtered MREG time domain signals are presented (blue), cardiorespiratory signals with $10 \times$ shorter window than the VLF/LF signals. Individual QPP_{maps} are presented next to corresponding physiological signals.

to be time locked to expiratory trough using a scanner pneumatic respiratory monitoring belt signal synchronized with the MREG sequence. For the LF and VLF waves, we detected periodic LF and VLF activity from the first peak from ICA time series of DMN_{vmpf} . We then used the QPP algorithm to automatically find high SNR events that spatiotemporally correlated in order to produce the respective LF_{map} and VLF_{map} images.

Averaging and phase locking of pulsation maps

The resulting averaged pulsation maps from the QPP analysis were then normalized into MNI coordinate space by using the FSL FLIRT transformation matrix that was obtained from initial anatomical registering. A whole-brain mask ($MNI152_T1_2mm_brain_mask$) was then used to exclude the signal outside of the brain.

The WL time courses of averaged pulsation maps in the brain were temporally normalized to the averaged WL amongst nine subjects with spline interpolation on a voxel-by-voxel basis. Then, z-scores were calculated on the series. Moreover, to match the data in phase, the QPP's Z maps of subjects one to eight were circularly phase shifted to match subject # 9's data (Matlab's code: `circshift`), finding the time lag with maximum Pearson correlation coefficient r with subject # 9. Finally, we obtain group QPPs that were contributed by cardiac pulsations, respiratory pulsations, and spontaneous VLF/LF fluctuations among all nine subjects by averaging individual shifted Z-score maps.

Results

MREG signal dynamics were studied in relation to physiological triggering, i.e. heart, respiration, and VLF fluctuations using the QPP maps described above.

Cardiovascular pulse effect in brain – $Card_{map}$

On average, the cardiac pulse induces a 5.5 (std 1.3) % signal change in the brain, c.f. Figure 3. The spatial distribution of the signal change is not uniform and the highest signal changes occur in the vicinity of the major blood vessels and near the ventricles reaching up to 13% signal change. The signal change in cortex drops to 1.4–4%.

In general, ultra-fast BOLD scans like MREG have mean and maximal signal amplitudes on motor tasks shown to be 1.2–3 times higher in MREG than gradient-echo EPI. On our calibration motor task, the MREG signal increase was 3% and for visual task the signal increase was 4% on average (data not shown).^{30,31} Our calibration MREG measures indicate

a maximum averaged 2.4% signal change during 30 s breathhold task (data not shown). The cardiac cycle effects were validated from MREG data arterial ICA time courses and individual ROIs. Both ECG data and scanner SpO_2 fingertip monitor (SpO_2 data not shown) present identical cardiac frequencies matching with the MREG data, c.f. Figure 1.

The R-peak locked $Card_{map}$ MREG signal change over the whole cardiac cycle is presented in Figure 3.

Similar to Posse et al.,³⁰ we also detected a negative cardiovascular pulse effect some 200–300 ms after the systolic R-wave in the vicinity of major cerebral arterial branches, c.f. Figure 4. The $Card_{map}$ presents an opposite positive MREG signal in the brain cortex compared to the arteries during the arrival of the cardiovascular impulse. The opposite MREG signal changes between the peri-arterial areas and brain parenchyma prevail throughout the cardiac cycle in the $Card_{maps}$.

After the arrival of the cardiovascular impulse the MREG signal decrease extends into ventricles and areas around fourth ventricle in the brain stem and cerebellum. Then, the signal change propagates centrifugally from the third and lateral ventricles into the adjacent basal ganglia, caudate, thalamic nuclei, and cerebellum at around 7–800 ms. Then, the cardiovascular impulse effect continues at 900 ms, spreads from periventricular structures like the cingulate cortex towards the brain cortex and reaches its maximum spread around 1000 ms following systole. The cardiovascular MREG signal impulse extends from dorsal regions towards the frontal parts of the brain. After reaching the cortical edge, the cardiac cycle-related MREG signal change reduces in power while spreading over the entire brain cortex.

A positive counterbalancing MREG signal change follows the route of the initiating signal decrease in a cyclic manner every heartbeat. The counterbalancing positive change spreads from the arterial regions beginning around 8–900 ms and becomes the dominant signal change over the whole cortex some 1500 ms following the previous heart beat. During this time, the heart has already undergone a new systole and starts the cycle again. The time domain MREG signals changes representing cardiac pulses in various parts of the brain are presented in Figures 4 and 5. (see also Supplementary S1 for dynamic 3D video of the cardiac impulse)

Respiratory pulsation effect on $Resp_{map}$

The respiratory cycle induces on average a signal change of 5.9 (std 1.2) % in the MREG data. The most marked pulsation occurs in the brain stem with a 14.4 (std 2.7)% change on average, c.f. Figure 3. The respiratory-related signal in the ventricles is also between 7–9% and ranges

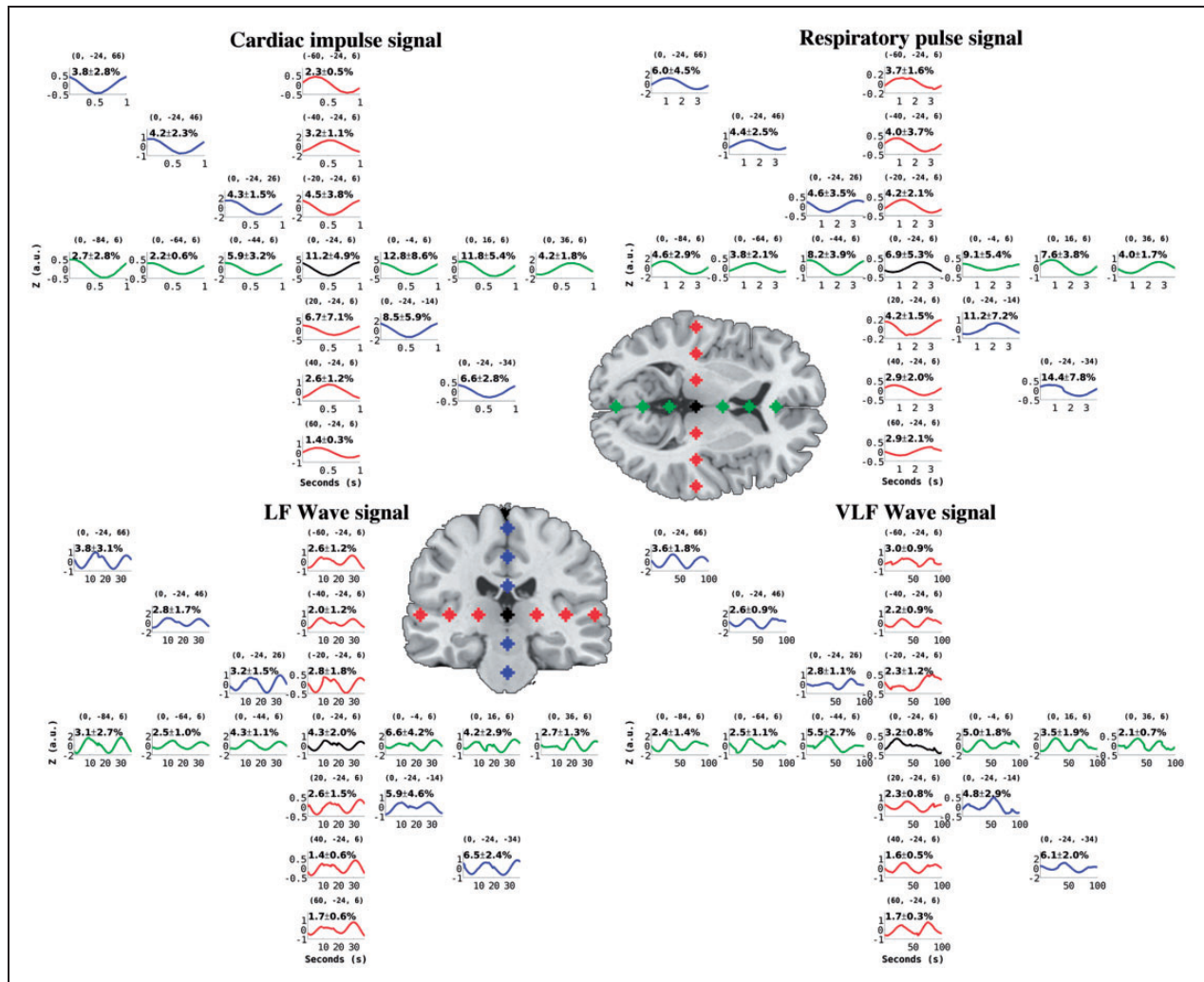


Figure 3. Group averaged time domain z-score signal change in the selected ROI's in 2 mm MNI space (coordinates in brackets) with in-plane T1-weighted image showing each ROI. Percent MREG signal change (\pm std) of the average regional pulse wave amplitude is shown in black. The cardiac impulse (top left) locked with the cardiac systole induces a markedly symmetric pulse between hemispheres and in the anterior–posterior direction but alters in phase in periarterial areas and in basal CSF areas near the circle of Willis. The respiratory (top right) pattern of the brain averaged into a 3.7 s cycle shows the slower effect to be more pronounced in cortical areas than in the white matter. The highest amplitudes were detected in pons and CSF areas. Quasi-periodic LF (37 s) and VLF (100 s time window) waves show the lack of temporal periodicity in basal areas and CSF areas but have more repeating pulsations in the cortex. Also note that all data are averaged and phase corrected to match subj # 9's QPP_{map} data.

between 3–6% in the brain cortex. The respiratory cycle MREG signal change map was triggered from a ROI in the corpus callosum (MNI 2 mm coordinates 0, –36, 14) since this area showed stable respiratory pulsations in individual respiratory frequencies around 0.25–0.4 Hz. There are also harmonic spectral power peaks in MREG data, e.g. the 1st harmonic frequency around 0.5–0.8 Hz, c.f. Figure 1. Synchronous scanner pneumatic respiratory monitoring belt data, as well as Aestiva/5 MRI monitor data (not shown) both validate the observed respiratory frequencies, c.f. Figure 1. Also note that the averaged respiratory effects are matched

to the subject # 9's relatively fast respiratory cycle of 3.7 s.

The respiratory cycle effects start to propagate centripetally at the beginning of the inspiration in peripheral brain regions as a positive MREG signal and alter into a negative one at the latter half of the cycle during exhalation. Similar to the cardiovascular impulse effect, the respiratory signal change also propagates from the back of the brain towards the front. The sagittal views in Figures 4 and 5 depict how the changes dominate around both below the sagittal sinus in the frontal brain and above the sinus rectus in the occipital

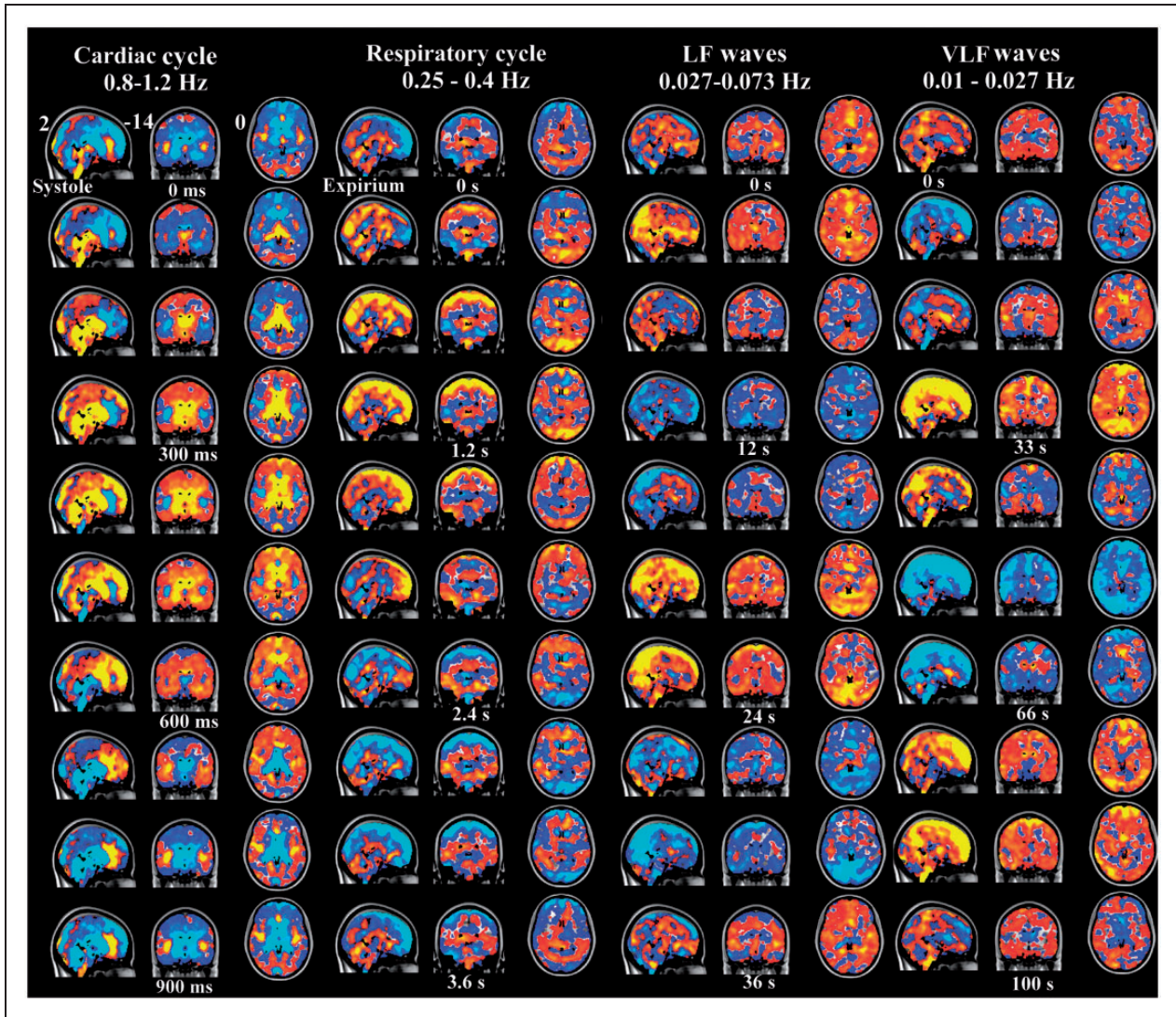


Figure 4. 3D time lapsed group averaged and phase-matched QPP_{maps} of physiological pulsations of the human brain. The cardiac impulse triggered by systole (ECG R-peak) shows a negative impulse starting from arteries and extending via ventricles into brain parenchyma. Next to cardiac is the respiratory cycle presenting a positive MREG signal change during inspiration. The LF and VLF waves are shown in 37 s and 100 periods matching DMN_{vmpf} signal sources, respectively. The color encoding represents normalized z-score from 0.05 to 1 yellow (negative in blue) in FSL MNI 152 2 mm space (x, y, z coordinates 0, 36, -14). For a better view of the dynamical nature of the pulsations, c.f. supplementary material S1 for 3D NI-video.

areas over the cerebellar tentorium, different from the cardiac cycle effect. Supplementary 3D video S1 presents the respiratory pulsations in a dynamical way.

The effects of respiration on the MREG data exhibit a cycle of positive changes followed by counterbalancing negative signal changes along the same spatial propagation direction. Spatially, the respiratory effect is clearly distinct from the cardiac cycle effect, c.f. Figures 3 and 4. The spatial effects of the respiratory cycle on MREG signal are more diffuse and global in the brain cortex than cardiovascular effects. The respiratory signal amplitudes are bigger in cortex of the brain than cardiovascular effects. Also the

cardiovascular changes have more of an impulse effect in nature with faster dynamics stemming from the arterial areas. The respiratory effect does not have the arterial changes preceding the cortical changes and moreover the arterial areas do not differentiate at all in $Resp_{maps}$.

During exhalation, the MREG signal is positive in white matter and ventricles in a quite symmetrical fashion between hemispheres. The MREG signal change in white matter is inverted compared to most of the cortex. Also the cerebellar hemispheres have an opposing MREG signal change compared to the cerebral cortex. However, areas adjacent to cerebellar vermis

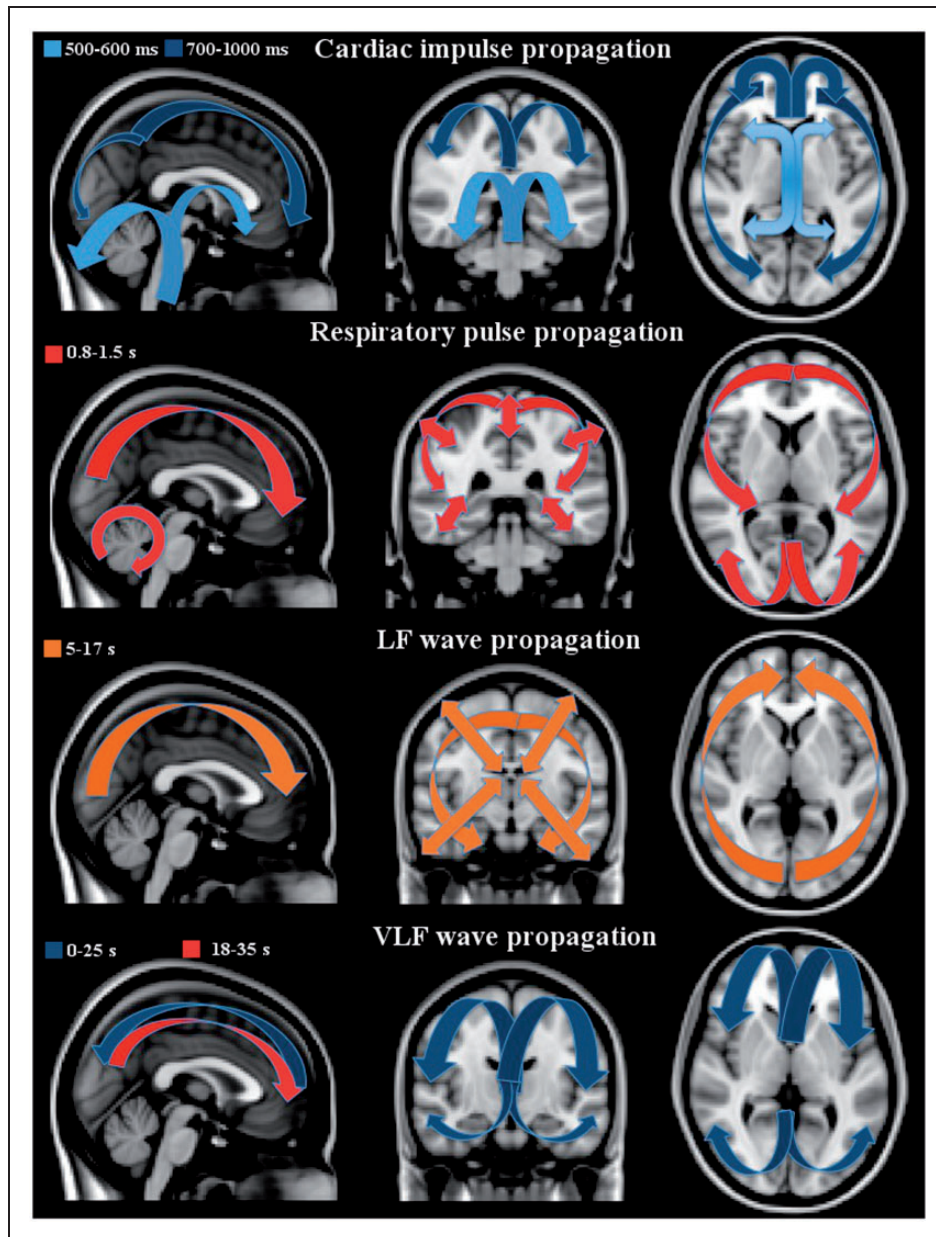


Figure 5. Anatomical MNI image with arrows pointing to the propagation direction of the first pulse effect, blue indicates negative and red-orange positive MREG-signal change. The cardiac impulse on top has timed negative post-systolic changes, which are cyclically followed by positive counter pulse effect in the same direction. The inspiration effects introduce a positive centripetal pulsation marked with double headed arrows. The LF waves induce wider and more uniform patterns extending to white matter. At the bottom, the VLF waves have both uniform, widespread pulses that intermittently mix with resting-state network patterns. Moreover, the VLF waves move in opposing directions compared to other pulses, c.f. initial blue wave going towards occipital areas followed by positive yellow direction towards the front.

and both thalami are in the same phase as the cerebral cortex. The respiratory signal change in the cerebellum seems to rotate in the sagittal plane in a clockwise manner, similar to cerebral sagittal changes as it advances towards the front. Both cerebral and cerebellar hemispheres present a draining type of signal change towards the sagittal sinus in posterior regions.

Vasomotor wave effects LF_{map} (0.027–0.073 Hz) and VLF_{map} (0.01–0.027 Hz)

The LF and VLF waves were individually triggered from random peaks but they were then phase corrected to match the waves originating from the first MREG signal peak from the anterior DMN_{vmpf} in subject # 9, c.f. Figure 1.

The averaged MREG percent signal change in the LF_{map} was 3.5 (std 0.7)% and VLF_{map} 2.4 (0.5)%, which is lower than the amplitude % change of the cardiorespiratory pulsations, c.f. Figure 3. The most marked changes in these frequencies can be depicted in the brain stem and ventricular areas, where the maximal average signal change is 7% in LF_{map} and 5% in VLF_{map} . In the cortex, the LF_{map} and the VLF_{map} signal change amplitude ranges from 1.7–4 % to 1–3%, respectively. The mean blood pressure fluctuations detected by MRI-compatible NIBP measurement data present specific spectral power peaks within both the LF and VLF ranges, similar to MREG spectral power changes c.f. Figure 2. In this study, we only analyzed the LF and VLF waves over a range of frequencies, but more specific analyses of the peak frequencies may bring more interesting results in the future.

The LF waves are spatially more widespread and temporally more complex than the more periodical cardiorespiratory pulsations, see also Figures 3 to 5 (dynamics of the LF waves in supplementary material S1). The LF MREG signal changes dominantly start from the parieto-occipital areas extending towards the frontal areas. Thereafter, the LF waves induce a positive MREG signal change covering symmetrically both hemispheres. Notably, the LF waves propagate more into the white matter than the cardiac and respiratory effects. The LF wave covers uniformly almost the whole brain.

The VLF pulsations are most complex in spatiotemporal dynamics. Initially, the VLF waves averaged to subject # 9's data are characterized by a very slow negative midline wave moving from frontal areas towards the back midline in the first 20–30 s. In contrast to all other physiological pulsations, the VLF wave then shows a reversed positive change going back from the occipital regions towards the front beneath the initial negative wave. All other pulsations have a cyclic behavior, where one change follows the other towards the same rotational direction after the previous change. The VLF waves also present intermittent resting state network configurations like salience, executive and default mode, and task positive networks mixed with global waves washing over the entire cortex.

Discussion

Our analysis based on ultra-fast MREG imaging shows that the human brain exhibits several distinct types of physiological pulsations. The cardiovascular pulsation induces a negative MREG signal centrifugal impulse followed by a positive change along the same route towards the cortex. Secondly, respiration-induced signal changes dominate in the cortex of the brain along the peri-venous collection system cycling centripetally towards the center of the brain. The third kind of pulsation of the brain are the VLF and LF waves that exhibit spatiotemporally

differential patterns; the LF waves have homogenous widespread repeating patterns, while the VLF waves are more quasi-periodic with complex RSN patterns repeatedly mixed with widespread waves. Of note, our analysis confirms and extends the previous fMRI observation of LF (quasi-periodic) pulsations slowly moving in the brain. The VLF/LF waves are indeed real independent phenomena and not aliased cardiorespiratory pulsations of fast cardiac activity that theoretically might have been aliased in previous studies.^{17–19}

The physiological pulsations shown in this paper are in agreement with glymphatic dynamics of CSF in the brain. The glymphatic draining system may be dysfunctional in clearing out protein debris in neurodegenerative diseases. A clinical platform capable of evaluating glymphatic pulsation mechanisms such as ultra-fast MREG in this study might open new possibilities in understanding the pathophysiological mechanisms behind glymphatic decline and protein accumulations in aging.³²

Cardiovascular brain impulse propels CSF centrifugally

The cardiovascular pulse induces a *negative* centrifugal MREG signal impulse in the brain. Posse et al.^{30,33} also detected a negative signal in an arterial ICA component with another ultra-fast MRI VEPI sequence. The negative change is strong in CSF and thus cannot be solely a classical BOLD susceptibility change. Moreover, in-flow effects would rather result in positive in signal changes³³ and would in any case not be expected given the 3D MREG excitation. The negative signal changes are more likely due to a disruption of steady-state precession caused by CSF impulses, which lead to incomplete T2 relaxation.^{34,35}

Pulsation-related de/accelerations of CSF are likely to contribute to the MREG signal, since the CSF convection within the glymphatic system exceeds normal water diffusion rates.¹ Near peri-arterial CSF areas, the MREG signal changes are large exceeding 10%, while in the cortical areas the amplitude of the cardiovascular impulse effect reduces to a level more typical of classical BOLD signal, i.e. to 2–5%. This implies a reduction in the CSF impulse effect in the tissue towards the periphery. This may be due to absorption of impulse effect by the glymphatic system in the brain tissue. Moreover, the oxygenation-related susceptibility changes might start to dominate in the MREG signal in the cortex. Also note the 3D videos that best illustrates the impulse type fast MREG change in the brain, c.f. supplementary S1.

Concomitant near-infrared spectroscopy (NIRS) measurements from the frontal brain cortices confirm an oxygenation impulse in the brain²³ and

differentiation of deoxy and oxyhemoglobin effects from CSF pulsations effects can be made in the future. The cardiac effects on grey matter BOLD signal have been monitored in the past mostly via analyzing the slow changes in the heart rate envelope with respect to classical 2 s TR BOLD signal.^{7–9,13,36,37} Our findings from ultra-fast MREG signal provide a new platform for the use of critically sampled ultra-fast MRI signal, to directly study fast cardiovascular pulsation dynamics in the human brain tissue beat by beat.²³

Respiration induces a centripetal counterpulsating MREG signal change

The venous flow of the brain is governed by two mechanisms; arterial perfusion modulations and by counterpulsation effects formed by the respiratory pressure changes within the thoracic cavity.³⁸ The respiratory rhythm-related MREG signal pulses are several times slower and lack the inverted arterial initialization that the cardiovascular impulse has. In fact, the respiratory pulsation initiates from peri-venous drainage areas in the cortical regions and propagates in a centripetal direction towards the brain center, which is opposite to the cardiovascular impulse effect. As only 15–20% of the propulsive energy of the glymphatic system originates from the cardiovascular pulsation, our results indicate that a counter-pulsation mechanism may occur during the respiratory cycle.³⁸ The respiratory pulsation acts as a low-pressure counter pulsating system that propels fluid and may act against debris accumulations in the peri-venous areas. In essence, glymphatic fluid efflux will drive accumulation of waste products into the peri-venous areas and subsequently out of the brain.

Inspiration increases and exhalation reduces venous outflow from the brain in the low-pressure venous drainage system.³⁸ Inspiration reduces blood volume in veins, increases peri-venous space, and opens room for glymphatic CSF outflow from the interstitial tissue. Inspiration also reduces venous deoxyhemoglobin levels due to out-flow, which in part may explain the related MREG signal increases. Exhalation reverses these effects; intra-thoracic pressure increases, veins distend increasingly, and peri-venous space closes leading to diminished glymphatic system drainage of CSF into peri-venous space. Furthermore, deoxygenated blood accumulates and by a combined effect of the previous events, the respiratory exhalation is correlated with a reduction in MREG signal.

The whole-brain BOLD signal effects of the respiratory cycle have not been previously addressed breath to breath due to technical limitations. However, it is widely accepted that slow changes in respiration volume and CO₂-levels have a strong effect on the BOLD signal especially in areas most metabolically active in resting

conditions, i.e. within the DMN.^{13,39,40} Furthermore, in line with our results, another recent ultra-fast, high-resolution MRI imaging also suggests that respiration indeed forms a major source of CSF flow.⁴¹

VLF/LF waves form complex and dynamic spatiotemporal effects

The original theories on the physiological background of the spontaneous BOLD signal fluctuations in low frequencies resting state suggest a strong link with vasomotor waves.^{7,8,16,42} However, currently the widest agreement for the source of LF BOLD fluctuations in functionally connected brain regions (or networks) is electrophysiological activity coupled with neurovascular activity.^{19,23,43–45}

The previously detected quasi-periodic pulsations seem to be reminiscent of VLF/LF vasomotor waves that in theory could influence glymphatic convection of CSF. As the arterial wall pressure clearly affects the convection of CSF into the brain,⁴⁶ slow waves in vasomotor tone, i.e. in the contractibility of the vessel wall smooth muscle cells, affects the glymphatics CSF pulsation as well. These baseline slow waves can be also detected as slow drifts in the cortical artery's diameter.^{4,42}

Vasomotor waves are known to have two different frequency ranges with an exchange power peak around 0.03 Hz.^{24,25,47} The slower vasomotor activity < 0.03 Hz is related to both parasympathetic and sympathetic activity, while the faster component is quite exclusively related to parasympathetic activity of the autonomous nervous control of the brain circulation.⁴⁷ The LF seems to induce global uniform changes throughout the brain also incorporating white matter more than cardiorespiratory pulsations. The VLF waves have both widespread global changes mixed with alternating resting state network patterns and unique waves travelling in opposing directions. The temporal fluctuations of the LF and VLF waves are smoother in the brain cortex and more complex in the basal CSF areas.

However, as the neuronal activity itself is tightly coupled to vascular events, the sources of the BOLD signal power < 0.3 Hz can also be electrophysiological in origin. Interestingly, simultaneous MREG and DC-EEG measurements of the same subject indicated that the DC-EEG potential is fluctuating markedly in VLF range.^{19,23,44,48,49} The DC-EEG potential has a strong contribution from non-neuronal potential over the blood–brain barrier (BBB).^{19,23,44,48,49–51} It is unlikely that the permeability of the BBB oscillates in a healthy brain at even low frequencies, as its function is to provide a stable barrier between the brain cells and blood. We propose that fluctuation in the glymphatic fluid fluxes in the perivascular space surrounding the BBB could contribute to the slow DC-EEG potential oscillations.

Vasomotor waves alter arterial diameter and perivascular space volume, which in turn modulate perivascular space electrical conductance between interstitium and perivascular space. This hypothesis is supported by studies in animals showing a close link between very low-frequency electrical activity and the quasi-periodic BOLD patterns.^{19,52} Additional in-depth multimodal analysis on VLF brain fluctuations is clearly needed to establish their origin and potential functions in humans.

Conclusion

Based on novel ultra-fast MREG brain scans, we present evidence suggesting that three distinct pulsation mechanisms of the human glymphatic system co-exist. The fastest mechanism is the cardiovascular pulsation that originates from basal peri-arterial spaces around the circle of Willis and extends centrifugally out towards the brain cortex. The second mechanism is the respiration that dominates perivenous spaces near the cortex in a centripetal fashion. Thirdly, the slow vasomotor wave fluctuations both in VLF and LF frequencies have distinct spatiotemporal patterns. We document that these three types of pulsations can be separated using ultra-fast MRI techniques. The capability to image glymphatic pulsation mechanisms may provide early information in neurodegenerative disease mechanisms.

Funding

This study was supported by CSTI-SHOK SALWE WP302 Grant, Academy of Finland Grants 123772 & 275352, Chinese NFSC-Grant 81020108022, German Research Foundation Grant EXC1086.

Acknowledgements

The authors thank Niko Huotari and Lauri Raitamaa for the final analyses.

Declaration of conflicting interests

The author(s) declared no potential conflicts of interest with respect to the research, authorship, and/or publication of this article.

Authors' contributions

VK, YZ designed the study, VK, XW, VK, TK, TT, collected and VK, XW, VK, TK, TT, JA analyzed the data and VK, XW, VK, JA, PL, SK, YZ, TT, TK, JH, MN wrote the ms. PL and JH provided MREG sequence and SK enabled pulsation analysis tool for the study.

Supplementary material

Supplementary material (holding a video of cardiac, respiratory and LF pulsation on the brain in MNI 3D template) for this paper can be found at <http://jcbfm.sagepub.com/content/by/supplemental-data>

References

1. Nedergaard M. Neuroscience. Garbage truck of the brain. *Science* 2013; 340: 1529–1530.
2. Xie L, Kang H, Xu Q, et al. Sleep drives metabolite clearance from the adult brain. *Science* 2013; 342: 373–377.
3. Rennels ML, Blaumanis OR and Grady PA. Rapid solute transport throughout the brain via paravascular fluid pathways. *Adv Neurol* 1990; 52: 431–439.
4. Iliff JJ, Wang M, Zeppenfeld DM, et al. Cerebral arterial pulsation drives paravascular CSF-interstitial fluid exchange in the murine brain. *J Neurosci* 2013; 33: 18190–18199.
5. Louveau A, Smirnov I, Keyes TJ, et al. Structural and functional features of central nervous system lymphatic vessels. *Nature* 2015; 523: 337–341.
6. Thrane AS, Rangroo Thrane V and Nedergaard M. Drowning stars: reassessing the role of astrocytes in brain edema. *Trends Neurosci* 2014; 37: 620–628.
7. Kiviniemi V, Jauhiainen J, Tervonen O, et al. Slow vasomotor fluctuation in fMRI of anesthetized child brain. *Magn Reson Med* 2000; 44: 373–378.
8. Biswal B, Yetkin FZ, Haughton VM, et al. Functional connectivity in the motor cortex of resting human brain using echo-planar MRI. *Magn Reson Med* 1995; 34: 537–541.
9. Purdon PL and Weisskoff RM. Effect of temporal autocorrelation due to physiological noise and stimulus paradigm on voxel-level false-positive rates in fMRI. *Hum Brain Mapp* 1998; 6: 239–249.
10. Dagli MS, Ingelholm JE and Haxby JV. Localization of cardiac-induced signal change in fMRI. *Neuroimage* 1999; 9: 407–415.
11. Poncelet BP, Wedeen VJ, Weisskoff RM, et al. Brain parenchyma motion: measurement with cine echo-planar MR imaging. *Radiology* 1992; 185: 645–651.
12. Birn RM, Murphy K, Handwerker DA, et al. fMRI in the presence of task-correlated breathing variations. *Neuroimage* 2009; 47: 1092–1104.
13. Birn RM, Diamond JB, Smith MA, et al. Separating respiratory-variation-related fluctuations from neuronal-activity-related fluctuations in fMRI. *Neuroimage* 2006; 31: 1536–1548.
14. Fox MD, Snyder AZ, Zacks JM, et al. Coherent spontaneous activity accounts for trial-to-trial variability in human evoked brain responses. *Nat Neurosci* 2006; 9: 23–25.
15. Buxton RB. Dynamic models of BOLD contrast. *Neuroimage* 2012; 62: 953–961.
16. Kiviniemi V. Endogenous brain fluctuations and diagnostic imaging. *Hum Brain Mapp* 2008; 29: 810–817.
17. Majeed W, Magnuson M and Keilholz SD. Spatiotemporal dynamics of low frequency fluctuations in BOLD fMRI of the rat. *J Magn Reson Imaging* 2009; 30: 384–393.
18. Majeed W, Magnuson M, Hasenkamp W, et al. Spatiotemporal dynamics of low frequency BOLD fluctuations in rats and humans. *Neuroimage* 2011; 54: 1140–1150.

19. Thompson GJ, Pan W-J, Magnuson ME, et al. Quasi-periodic patterns (QPP): large-scale dynamics in resting state fMRI that correlate with local infraslow electrical activity. *Neuroimage* 2014; 84: 1018–1031.
20. Beall EB and Lowe MJ. SimPACE: generating simulated motion corrupted BOLD data with synthetic-navigated acquisition for the development and evaluation of SLOMOCO: a new, highly effective slice-wise motion correction. *Neuroimage* 2014; 101: 21–34.
21. Jacobs J, Stich J, Zahneisen B, et al. Fast fMRI provides high statistical power in the analysis of epileptic networks. *Neuroimage* 2014; 88: 282–294.
22. Assländer J, Zahneisen B, Hugger T, et al. Single shot whole brain imaging using spherical stack of spirals trajectories. *Neuroimage* 2013; 73: 59–70.
23. Korhonen V, Hiltunen T, Myllylä T, et al. Synchronous multiscale neuroimaging environment for critically sampled physiological analysis of brain function: heptascan concept. *Brain Connect* 2014; 4: 677–689.
24. Panerai RB, Rennie JM, Kelsall AW, et al. Frequency-domain analysis of cerebral autoregulation from spontaneous fluctuations in arterial blood pressure. *Med Biol Eng Comput* 1998; 36: 315–322.
25. Wagner CD and Persson PB. Two ranges in blood pressure power spectrum with different 1/f characteristics. *Am J Physiol* 1994; 267: H449–H454.
26. Zuo X-N, Di Martino A, Kelly C, et al. The oscillating brain: complex and reliable. *Neuroimage* 2010; 49: 1432–1445.
27. Cox RW. AFNI: Software for analysis and visualization of functional magnetic resonance neuroimages. *Comput Biomed Res Int J* 1996; 29: 162–173.
28. Cox RW. AFNI: What a long strange trip it's been. *Neuroimage* 2012; 62: 743–747.
29. Smith AM, Lewis BK, Ruttimann UE, et al. Investigation of low frequency drift in fMRI signal. *Neuroimage* 1999; 9: 526–533.
30. Posse S, Ackley E, Mutihac R, et al. Enhancement of temporal resolution and BOLD sensitivity in real-time fMRI using multi-slab echo-volumar imaging. *Neuroimage* 2012; 61: 115–130.
31. Safi-Harb M, Proulx S, von Ellenrieder N, et al. Advantages and disadvantages of a fast fMRI sequence in the context of EEG-fMRI investigation of epilepsy patients: a realistic simulation study. *Neuroimage* 2015; 119: 20–32.
32. Kress BT, Iliff JJ, Xia M, et al. Impairment of paravascular clearance pathways in the aging brain. *Ann Neurol* 2014; 76: 845–861.
33. Posse S, Ackley E, Mutihac R, et al. High-speed real-time resting-state FMRI using multi-slab echo-volumar imaging. *Front Hum Neurosci* 2013; 7: 479.
34. Zhao X, Bodurka J, Jesmanowicz A, et al. B(0)-fluctuation-induced temporal variation in EPI image series due to the disturbance of steady-state free precession. *Magn Reson Med* 2000; 44: 758–765.
35. Bhattacharyya PK and Lowe MJ. Cardiac-induced physiologic noise in tissue is a direct observation of cardiac-induced fluctuations. *Magn Reson Imaging* 2004; 22: 9–13.
36. Chang C, Cunningham JP and Glover GH. Influence of heart rate on the BOLD signal: the cardiac response function. *Neuroimage* 2009; 44: 857–869.
37. Tong Y, Hocke LM and Frederick BdeB. Short repetition time multiband echo-planar imaging with simultaneous pulse recording allows dynamic imaging of the cardiac pulsation signal. *Magn Reson Med* 2014; 72: 1268–1276.
38. Schaller B. Physiology of cerebral venous blood flow: from experimental data in animals to normal function in humans. *Brain Res Rev* 2004; 46: 243–260.
39. Wise RG, Ide K, Poulin MJ, et al. Resting fluctuations in arterial carbon dioxide induce significant low frequency variations in BOLD signal. *Neuroimage* 2004; 21: 1652–1664.
40. Chang C and Glover GH. Relationship between respiration, end-tidal CO₂, and BOLD signals in resting-state fMRI. *Neuroimage* 2009; 47: 1381–1393.
41. Dreha-Kulaczewski S, Joseph AA, Merboldt K-D, et al. Inspiration is the major regulator of human CSF flow. *J Neurosci* 2015; 35: 2485–2491.
42. Drew PJ, Shih AY and Kleinfeld D. Fluctuating and sensory-induced vasodynamics in rodent cortex extend arteriole capacity. *Proc Natl Acad Sci U S A* 2011; 108: 8473–8478.
43. Deco G, Jirsa V, McIntosh AR, et al. Key role of coupling, delay, and noise in resting brain fluctuations. *Proc Natl Acad Sci U S A* 2009; 106: 10302–10307.
44. Hiltunen T, Kantola J, Abou Elseoud A, et al. Infraslow EEG fluctuations are correlated with resting-state network dynamics in fMRI. *J Neurosci* 2014; 34: 356–362.
45. Hutchison RM, Womelsdorf T, Allen EA, et al. Dynamic functional connectivity: promise, issues, and interpretations. *Neuroimage* 2013; 80: 360–378.
46. Hadaczek P, Yamashita Y, Mirek H, et al. The 'perivascular pump' driven by arterial pulsation is a powerful mechanism for the distribution of therapeutic molecules within the brain. *Mol Ther* 2006; 14: 69–78.
47. Akselrod S, Gordon D, Ubel FA, et al. Power spectrum analysis of heart rate fluctuation: a quantitative probe of beat-to-beat cardiovascular control. *Science* 1981; 213: 220–222.
48. Ko AL, Darvas F, Poliakov A, et al. Quasi-periodic fluctuations in default mode network electrophysiology. *J Neurosci* 2011; 31: 11728–11732.
49. Chow HM, Horovitz SG, Carr WS, et al. Rhythmic alternating patterns of brain activity distinguish rapid eye movement sleep from other states of consciousness. *Proc Natl Acad Sci U S A* 2013; 110: 10300–10305.
50. Voipio J, Tallgren P, Heinonen E, et al. Millivolt-scale DC shifts in the human scalp EEG: evidence for a non-neuronal generator. *J Neurophysiol* 2003; 89: 2208–2214.
51. Nita DA, Vanhatalo S, Lafortune F-D, et al. Nonneuronal origin of CO₂-related DC EEG shifts: an in vivo study in the cat. *J Neurophysiol* 2004; 92: 1011–1022.
52. Pan W-J, Thompson GJ, Magnuson ME, et al. Infraslow LFP correlates to resting-state fMRI BOLD signals. *Neuroimage* 2013; 74: 288–297.